Improving Earth Background Characterization Through Modeling and Measurements of Leaf Bidirectional Reflectivity

Shadrian B. Strong, Michael E. Thomas, Andrea M. Brown, and Elena Y. Adams

The Earth albedo, or the ratio of the upwelling to down-welling radiative flux at the surface, consolidates both wavelength- and angle-dependent information, often oversimplifying surface properties. Accurate characterization of this parameter is important for many Johns Hopkins University Applied Physics Laboratory (APL) programs. Within the albedo value is the bidirectional reflectance distribution function (BRDF), which describes the angle dependency of reflectance and emission relative to observation angle, solar angles, and wavelength. As a first step toward improving land characterization of Earth and assisting with removal of land radiative effects to reveal pristine target signatures, we developed a semiempirical BRDF model for leaves. Leaves are easy to acquire, easy to integrate into an existing facility, and highly seasonally and regionally dependent. Typical leaf reflectances used in modeling cover a wavelength of ~500–2000 nm. We extended this database from 250 to 10,000 nm to examine the radiative impact of surface albedo. In this article, we present the model and compare it with quantitative observations for red maple, dogwood, and white oak leaves. Implementing the default parameterization of a maple leaf in the Moderate Resolution Radiative Transfer (MODTRAN) radiative transfer code results in a retrieved radiance error of 1–3% relative to our improved BRDF model. This error is outside the required absolute accuracy for environmental and atmospheric models used at APL and highlights the need to use our new parameterization for environmental studies.

INTRODUCTION

Reflected solar radiation from Earth is directly measurable by satellite instrumentation. The reflectance observed by a spacecraft sensor contains both surface and atmospheric components and depends on the direction of solar illumination and angle of observation. Whether the observational intent is to gather infor-

mation about the atmosphere specifically or to identify embedded surfaces or targets, decoupling the effects of these contributions is critical to accurately deriving thermal and intensity information for objects of interest. As discussed by Hudson et al.,[1] this decoupling is challenging because the atmospheric and surface interaction comprises multiple scattering effects.

It is critical to extricate atmospheric, surface, and target properties for a broad range of applications. For example, both Johns Hopkins University Applied Physics Laboratory (APL) Air and Missile Defense and National Security Space Mission Area applications require accurate, radiometric characterization of specific man-made targets. Physical changes in the target (e.g., material, temperature, and emissivity changes) must be disentangled from the physical changes of Earth's background. Neglecting changes in the atmosphere or environment may result in attributing natural variability to changes in the target. Ignoring surface scattering and reflection properties has led to uncertainties as high as 15–20% in radiance and surface brightness retrievals.[2] For APL's Civil Space Mission Area, it is essential to distinguish between short-term (hourly, daily) cloud reflection and long-term (seasonal, annual) ice reflection.[3] This knowledge of surface reflectivity, input into general circulation models for climate change investigation, has a substantial impact on model predictions.[4] In particular, assumed land surface reflectivity directly affects global surface energy and water balance in these simulations. Deviations between satellite observations and model assumptions of surface reflectivity reveal errors >25% in surface reflectance.[5]

The percent reflection of Earth, as viewed by a satellite, is referred to as albedo, or the ratio of the upwelling to down-welling radiative flux at Earth's surface. The albedo is related to the integral of the wavelength-dependent bidirectional reflectance distribution function (BRDF), which describes the angle dependency of reflectance (and emission) relative to observation angle and solar angles. Often, the intrinsic BRDF of a surface is lost in the observation of a single-value albedo because the albedo is a summation or angle-averaged BRDF. There is also an inherent loss of spectral dependency in albedo. Little has been done to quantify the impact of subtle changes in BRDF on the derivation of albedo, but it has been shown that small changes in albedo (<10%) result in large thermal changes (>80%).[6] An absolute accuracy of 0.02–0.05 for albedos is required for climate, biochemical, and hydrological models (e.g., Ref. 6). Models used at APL through NASA Earth science programs require this accuracy to assess anthropogenic and nonanthropogenic contributions to the Earth climate system. APL's National Security Space and Air and Missile Defense Mission Areas require this accuracy to assess the radiative signature of the atmosphere on target detection, identification, and signature analysis.

Earth surface BRDFs are highly dependent on land surface characteristics, including vegetation type (or lack thereof), soil, moisture, and physical state (solid, liquid, gas). BRDFs, and consequentially albedos, may be physically modified through seasonal changes, anthropogenic particulate deposition (such as soot, aerosols, etc.), agricultural practices, deforestation, urbanization, and daily meteorologically driven actions (wind, erosion, etc.). As the radiometric interface between the land surface and the atmosphere, the albedo both defines the lower boundary for atmospheric radiative transfer and details the total shortwave energy input into the biosphere.[7] Surface albedo is an important parameter used to investigate the net change between incoming radiation energy and outgoing radiation energy in the Earth climate system (e.g., Ref. 7). At the most basic level, understanding changes in the BRDFs of a variety of natural surfaces (e.g., leaf/tree type, ice, sand, rock) will enable more accurate derivations of surface albedos.

As a first step toward creating an improved database of natural Earth surface BRDFs for use in APL National Security Space and Civil Space Mission Area

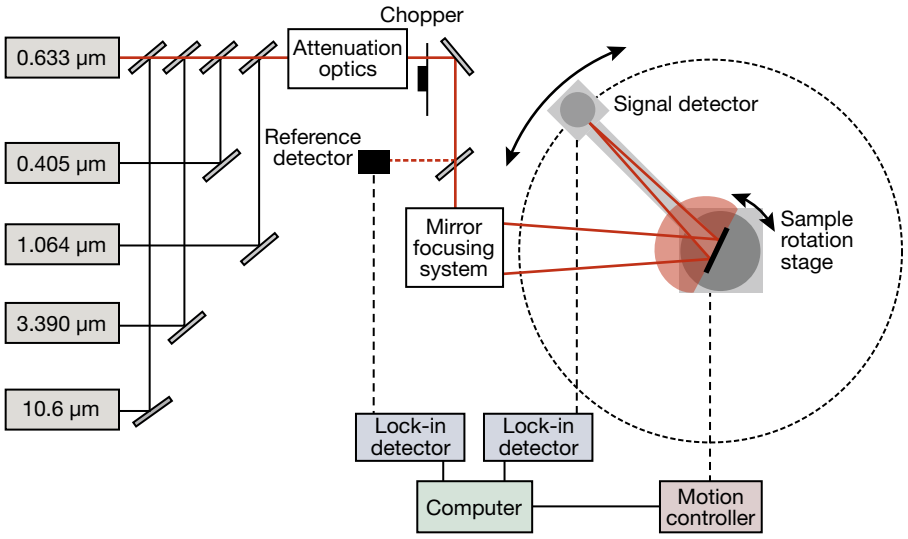

Figure 1. Experimental setup of the AMD BRDF system. Inputs are five laser sources shown on the left. Inputs travel through a series of optical components (middle). Shown on the right is the position of the sample on a rotating stage and mobile sensor unit. Reproduced from Ref. 15. © 2010 Society of Photo Optical Instrumentation Engineers.

applications, we have developed a semiempirical BRDF model for leaves using the APL Air and Missile Defense Sector's BRDF laboratory facility with parameters from the Leaf Optical Properties EXperiment (LOPEX) database.[8] Sponsored jointly by APL National Security Space Mission Area and Research and Exploratory Development Department independent research and development funding in 2009, we developed a model for leaves specifically, but the model has potential for broad application. Leaves are easy to acquire, easy to integrate into the existing APL facility apparatus, and highly seasonally and regionally dependent. They cover ~10% of Earth.

By investigating BRDF variability in leaves as a function of species, water content, chlorophyll content, and thickness, we begin to understand how a more complex system, such as a tree or canopy, may be parameterized. An initial simple analysis of the BRDF of individual leaves is required before we can extrapolate and study the signatures of trees and forests: we anticipate the BRDF of entire trees and forests would be highly complex and variable but would maintain an underlying signature associated with plant type. Leaf reflectance is partly due to roughness with varying density, dimension, and refractive indices and partly due to scattering off cell surfaces.[9] The leaf is the primary energy-harvesting element of a plant and provides the energy necessary to drive the conversion of CO_2 into plant sustenance.[10] Remote sensing observations of changes in leaf reflectivity and emission can provide information about plant type (e.g., detection of invasive plant species)[11] and information about changes in ecosystems (e.g., Ref. 12). We have compared our model and observations with the Leaf Experimental Absorptivity Feasibility MODel (LEAFMOD)[10] and found them to agree favorably. We have parameterized leaf BRDFs for the 0.3- to 3.5-μm wavelength range for deciduous leaves: maple, dogwood, and oak leaves. We anticipate deciduous tree leaves to have simpler BRDFs, facilitating preliminary analysis. Further study would incorporate coniferous species. The leaf parameterization has been implemented for inclusion in the Moderate Resolution Radiative Transfer (MODTRAN) model.[13]

EXPERIMENTAL SETUP

The Air and Missile Defense Sector's BRDF laboratory system is shown in Fig. 1. The system is typically used to analyze the scattering from man-made surfaces such as ceramics, paints, and metals. There are currently many laser wavelengths available for measurements from UV to the longwave infrared (LWIR), although only five are depicted in Fig. 1. Free-space mirrors are used to manually select the wavelength of interest for each series of measurements. A lock-in detector is used to separate the reflected signal from background light, and a chopper is used in the path of the continuous wave lasers for this purpose. Mirrors are used to focus the laser light onto the signal detector, which is mounted on an extension arm attached to a rotation stage. The sample is placed in the center of the detector circle on the second rotation stage, which controls the incident angle of the laser light. The leaf specimen is vertically attached to the second rotation stage (Fig. 2). Figure 1 depicts the layout of the BRDF facility

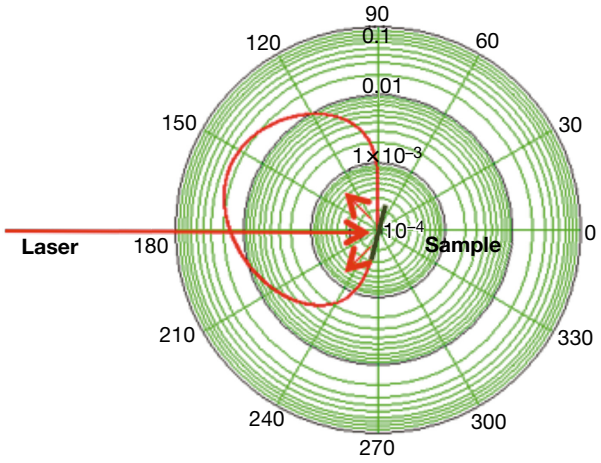

Figure 2. The leaf specimen is vertically attached to the rotation stage in the center of the apparatus. The laser beam is then incident on the sample, and the resultant reflection/scatter is measured at the detector.

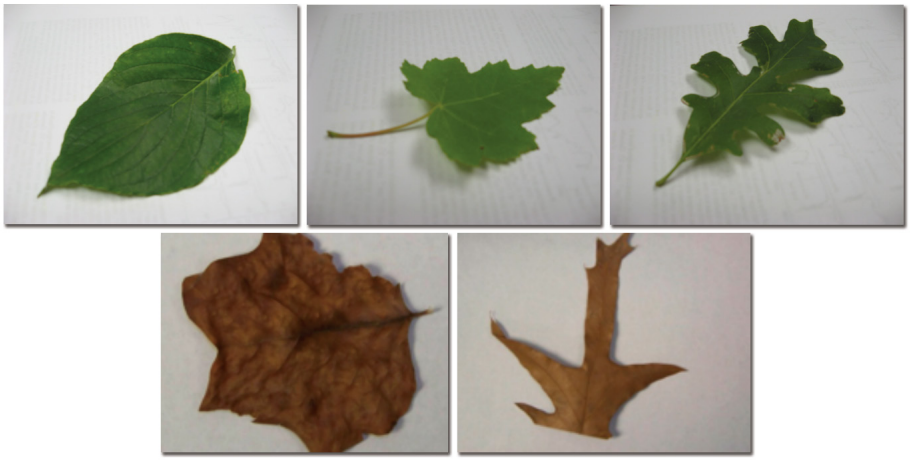

Figure 3. Spring/summer flowering dogwood leaf (top left), red maple leaf (top center), and white oak leaf (top right) and fall maple leaf (bottom left) and oak leaf (bottom right).

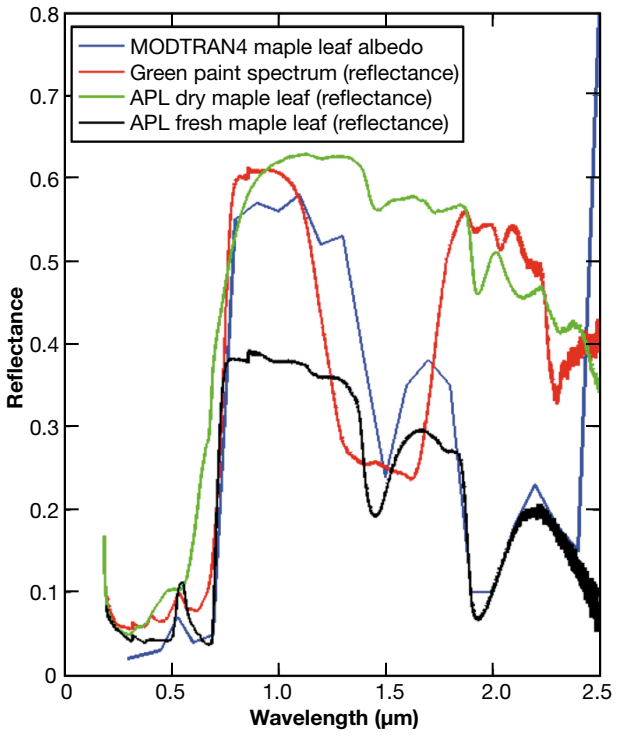

Figure 4. Spectrum of the default MODTRAN4 maple leaf reflectance (blue), spectrum of a green paint sample (red), dry maple leaf reflectance spectrum (green), and fresh maple leaf reflectance spectrum (black). Notably, the dry and fresh samples have distinctly different chlorophyll "red edges" near 0.750 μm, such that the dry leaf (green) has a smoother slope between 0.5 and 1 μm relative to the sharp, near-discontinuity of the fresh leaf (black). Differences in water content and leaf thickness account for amplitude changes. The MODTRAN4 spectrum has a coarser resolution and does not enable the model user to differentiate between dry and fresh leaves. For comparison, we have included a green paint sample, which mimics features of the leaves, including the chlorophyll bump near 0.5 μm.

with some of the available laser wavelengths represented. A current list of available wavelengths includes: 0.375, 0.405, 0.532, 0.633, 0.635, 0.760, 0.830, 0.905, 1.064, 1.55, 3.39, and 10.6 μm and a scanning optical parametric oscillator that includes wavelengths from 1.4 to 1.9 and 2.4 to 3.8 μm. APL recently acquired a vacuum chamber with optical ports spaced at 20° increments in the scattering plane. This chamber facilitates the measurement of high-temperature BRDFs using either a resistive heating element to heat the sample from the back or a 40-W CO_2 laser to heat the sample from the front.

Three different species of leaves were analyzed: (*i*) red maple (*Acer rubrum*), (*ii*) flowering dogwood (*Cornus florida*), and (*iii*) white oak (*Quercus alba*), shown in Fig. 3. Leaf samples were collected from APL's main campus. Both "fresh" and dry leaves were analyzed. In the case of fresh leaves, a sample from each of the species was selected immediately before measurements were to be conducted. This was done to ensure that minimal water was lost (due to drying of the leaves and decomposition). Loss of water was shown to affect the observed absorption and reflectance spectrum. This may be observed in Fig. 4 (green for dry maple leaf and black for fresh maple leaf). For comparison, green paint is overplotted in red, and the assumed MODTRAN maple leaf spectrum is overplotted in blue. Notably, the dry maple leaf exhibits both a high reflectance relative to the fresh leaf and a degradation in the chlorophyll feature near 500 nm. The MODTRAN spectrum most closely replicates the green-paint spectrum and neither of the two maple leaf samples. Angle-resolved reflectance data were collected for each sample at three different sample rotary angles at wavelengths of 405, 633, 1064, and 3390 nm.

Spectrally resolved total integrated reflectance [TIR; also called hemispherical directional reflectance (HDR)] and transmittance [also called hemispherical directional transmittance (HDT)] data were also collected for each leaf species by using a grating spectrometer to cover the UV, visible, and near-infrared (NIR) regions of the spectrum, and a Fourier transform infrared spectrometer was used to cover the midwave infrared (MWIR) and LWIR regions of the spectrum.

BRDF MODELING

The BRDF is defined as the ratio of backward-reflected flux into the differential solid angle, Ω_r, to the incident flux, Ω_i,

$$\rho(\Omega_i, \Omega_r, \omega) = \frac{1}{\Phi_i}\frac{d\Phi_r}{d\Omega_r} = \frac{I_r(\Omega_i, \Omega_r, \omega)\hat{\boldsymbol{\varepsilon}}_r \cdot \hat{\mathbf{n}}}{\Phi_i(\omega)} . \quad (1)$$

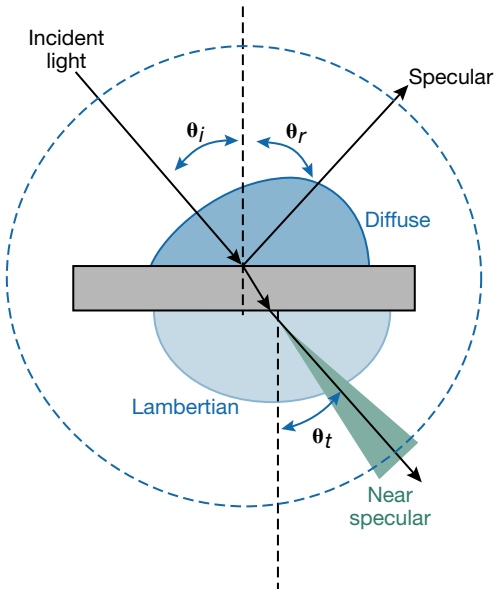

Figure 5. Experimental geometry and graphical depiction of scattering models for in-plane measurements. Reproduced from Ref. 15. © 2010 Society of Photo Optical Instrumentation Engineers.

$\rho(\Omega_i,\Omega^r,\omega)$ is called the BRDF. For a flat reflecting surface, $\hat{\boldsymbol{\varepsilon}}_r \cdot \hat{\mathbf{n}} = \cos\theta_r$. The inner product equals 1 for a spherical surface or a point reflector.

For a homogenous, uniform surface with randomly oriented surface roughness, the BRDF will display no dependence in the φ direction (out of the plane reflection). Consequentially, scatter from the sample is unchanged under rotation by the angles φ_i and φ_r, and the phase function is a function of θ_i and θ_r only. This is assumed to be the case for the samples analyzed in this study, and all measurements and analyses are performed for in-plane scatter (i.e., the case of $\varphi = 0°$).

Integrating the BRDF over the entire hemisphere results in the hemispherical TIR (also called directional hemispherical reflectance), ρ_{TIR}. The values of ρ_{TIR} range from 0 to 1. The modeled BRDF is a product of the TIR and a normalized angle-dependent phase function, $P(\theta_i,\theta_r)$. All phase functions are normalized to 1, becoming equivalent to a probability density function, such that one may determine the probability of observing a scattered ray in a particular direction given an incidence angle. The BRDF may be written as

$$BRDF(\theta_i,\theta_r) = \rho_{TIR}(\theta_i)P_r(\theta_i,\theta_r). \tag{2}$$

Physically based empirical models are fit to the BRDF experimental data to extend a limited set of in-plane scattering data to all possible incident and scattered angles. The model also compensates for the dropout in experimental signal caused by the detector arm blocking the incident laser beam from striking the sample for a small range of scattering angles (see Fig. 10). The BRDF model is separated into specular (*S*), near-specular (*NS*), diffuse (*D*), and Lambertian (*L*) components. Each of these four components follows a separate angular dependence [P(θ)] and together represent the reflected beam from the interface reflection (specular) and the surface and bulk scattered light.[14] The BRDF is modeled as a sum of all four components, in other words,

$$\begin{aligned} BRDF(\theta_i,\theta_r,\lambda) = {} & \rho_S(\theta_i,\lambda)P_{inst}(\theta_i,\theta_r,\lambda) + \rho_{NS}(\theta_i,\lambda)P_{NS}(\theta_i,\theta_r,\lambda) \\ & + \rho_D(\theta_i,\lambda)P_D(\theta_i,\theta_r,\lambda) + \rho_L(\lambda)P_L(\theta_r,\lambda). \end{aligned} \tag{3}$$

It is assumed that these different types of reflected, transmitted, and scattered light are independent. Specular components (P_S) represent the contributions from the

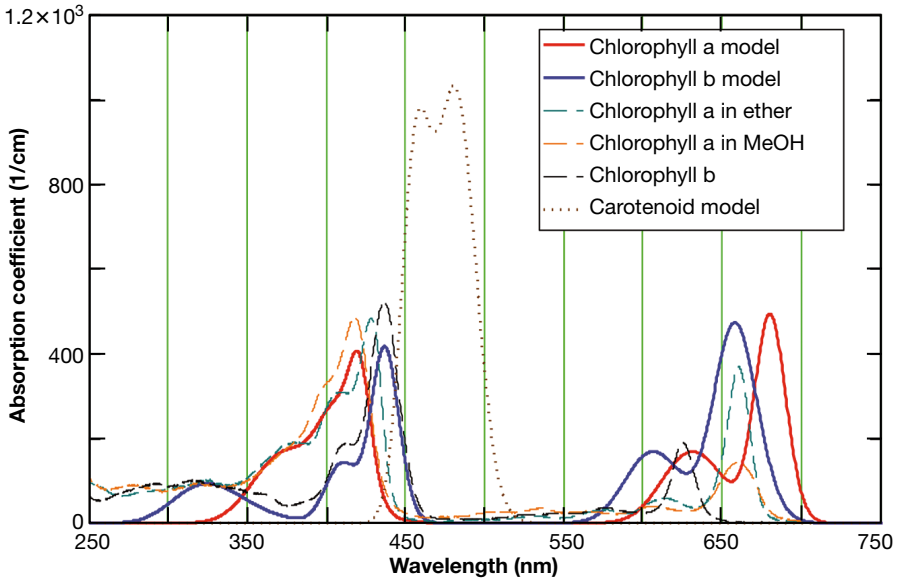

Figure 6. Comparison of chlorophyll a and b absorption coefficient to uncalibrated published spectra.

reflected and transmitted rays for a perfectly flat surface and are calculated by applying the Law of Reflection (i.e., $\theta_r = -\theta_i$). Near-specular components (P_{NS}) represent weak or single scatter phenomena that are only slightly spread from the specular direction primarily because of minor surface roughness. Diffuse components (P_D) represent the effects of surface roughness and bulk scatter that are strongly influenced by multiple scatter and are partially coherent relative to the incident light. The Lambertian components (P_L) represent random rough surface and bulk scatter that is entirely incoherent with the incident light.[15] Examples of all four types of reflection are depicted in Fig. 5. Because of the diffuse nature of the samples studied, only the diffuse and Lambertian components are required to model the reflectance from the three species of leaves that were studied.

The diffuse phase function is given by

$$P_D = (\theta_r, \theta_i, m, \alpha) = N_D \frac{(\alpha \cos\theta_i)^{m-1}}{(\sin\theta_r + \sin\theta_i)^m + (\alpha \cos\theta_i)^m} \cos\theta_r, \tag{4}$$

where α is the half angle of the reflected beam, m is an exponent chosen to best fit the observed data, and N_D is a normalization factor.[15–17] The hemispheric Lambertian phase function is given by

$$P_L(\theta_r) = \frac{1}{\pi} \cos\theta_r. \tag{5}$$

The integrated quantities for each component represent the fraction of incident light that is reflected under each phase function. The TIR for the entire BRDF would then be the sum of each individual component integrated reflectances, or

$$\rho_{TIR}(\theta_i, \lambda) = \rho_L(\theta_i, \lambda) + \rho_D(\theta_i, \lambda) + \rho_{NS}(\theta_i, \lambda) + \rho_S(\theta_i, \lambda) \leq 1. \tag{6}$$

The TIR for the complete BRDF follows the total power law,

$$1 = (\rho_{TIR}(\theta_i, \lambda) + \rho_{TIT}(\theta_i, \lambda)) + \alpha_{abs}(\theta_i, \lambda) = \rho_{TIS}(\theta_i, \lambda) + \alpha_{abs}(\theta_i, \lambda), \tag{7}$$

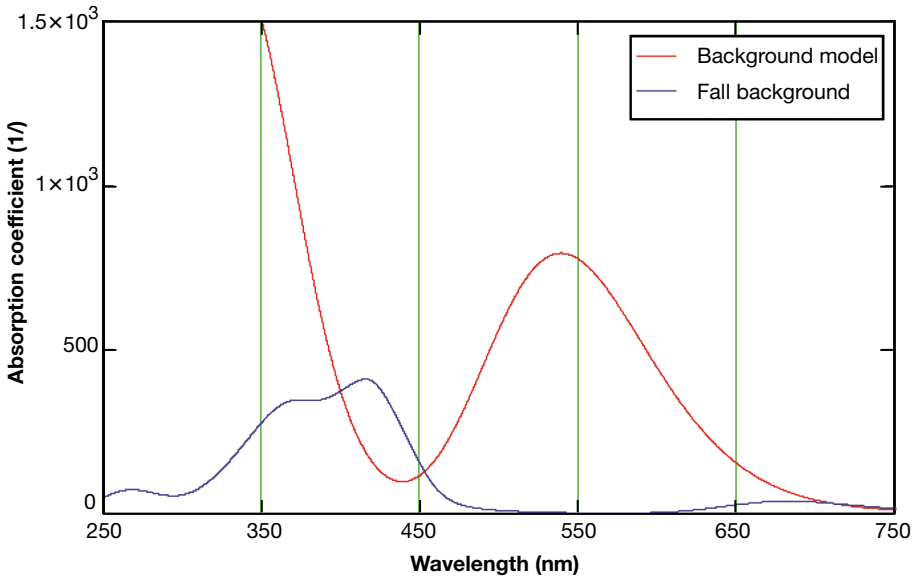

Figure 7. Required background absorption to fit observed leaf spectra. The fall leaf background is mostly due to decomposing chlorophyll.

Table 1. Content of different species composing the leaf absorption coefficients as implemented in the APL model for maple, dogwood, and white oak

Sample	Water	Chlorophyll	Dry leaf matter	Carotenoids	Decomposing chlorophyll	Concentration of scatter centers (no. per cm^3)	Scatter radius (mm)	Leaf thickness (cm)
Fall red maple	0.135	0.005	0.09	0.1	0.67	2.9×10^8	1.95	0.015
Fall white oak	0.135	0.005	0.09	0.1	0.67	2.9×10^8	1.95	0.037
Spring dogwood	0.6	0.27	0.03	0.1	0	0.75×10^8	1.7	0.033
Spring holly	0.6	0.27	0.055	0.075	0	0.75×10^8	1.7	0.037

Mixing ratios listed by concentration. The listed radius is for an effective sphere.

where ρ_{TIT} is the total integrated transmittance, ρ_{TIR} is the TIR, and α_{abs} is the absorptance. Following Kirchhoff's law of thermal radiation, the emissivity (ε) of a material is equal to its absorptance, therefore

$$\varepsilon(\theta_i,\lambda) = 1 - (\rho_{TIT}(\theta_i,\lambda) + \rho_{TIR}(\theta_i,\lambda)) = 1 - \rho_{TIS}(\theta_i,\lambda). \quad (8)$$

The BRDF for the leaves, or any opaque material, provides an estimate of the unidirectional emissivity of a material at a particular incident angle and wavelength.[15,17]

The Lambertian BRDF model is a variation on a radiative transfer model with a two-stream approximation (see the *Appendix* A for further description). The model uses the Kubelka–Munk equation to account for the relationship between absorption concentration and reflectance in the leaf specimens, modeling the wavelength-dependent reflectance and transmittance of the leaf. The model takes as input four leaf constituents that act as the main absorbers in the leaf samples: chlorophylls (types a and b), water, carotenoids, and background material or "dry leaf matter." Figures 6 and 7 plot the absorption coefficient of these constituents. The model is designed such that the absorption coefficients of each of the leaf components may be varied to fit the measured data from the UV through the LWIR. The mixture coefficients used for each different tree species can be found in Table 1. The fall leaf background is believed to be decomposing

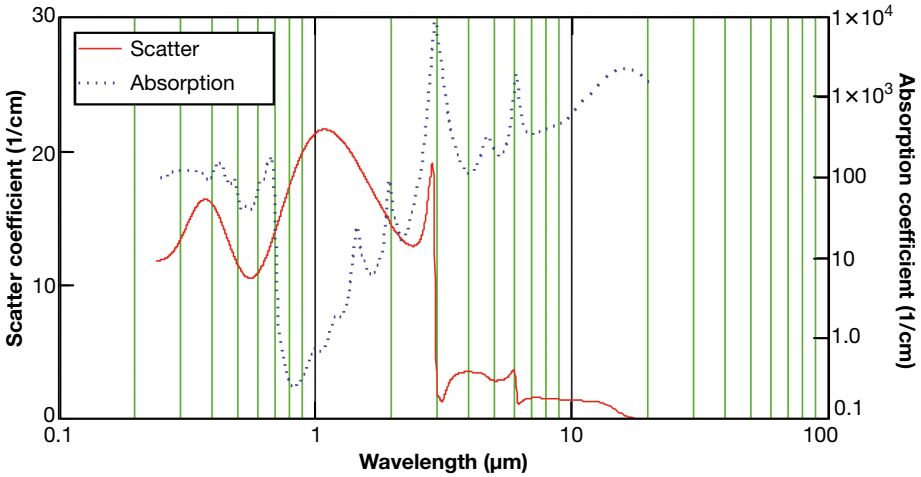

Figure 8. Scatter coefficient and net absorption coefficient for a spring/summer green leaf.

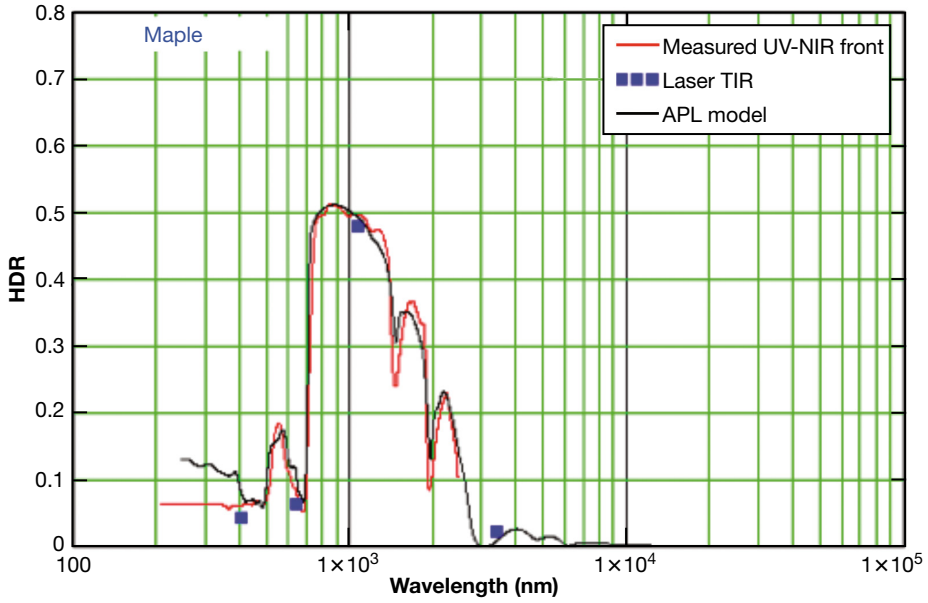

Figure 9. The APL leaf model fit (black) to the spectrometer measurements (red). The BRDF TIR measurements for the spring red maple are overplotted with blue squares.

chlorophyll. Also listed in Table 1 are the leaf thickness, the most common particle radius, and the number of scatter centers within each leaf. This information is used to compute the scatter coefficient based on anomalous diffraction approximation (ADA). For this calculation, it is assumed that the particles are spherical. It is interesting to note that the size of chloroplasts within a leaf cell match the size of the scattering particles required by the model. The index of refraction of the scattering particles is assumed to be 1.6. For green leaves, the background is predominantly water. The combination of Kubelka–Munk theory and ADA make this approach computationally efficient. A plot of the scatter coefficient and net absorption coefficient for a spring/summer leaf is presented in Fig. 8. A measured TIR spectrum is then used to empirically determine these parameters for each leaf. An example of the fit obtained by using this model is shown in Fig. 9 for a spring maple leaf.

The TIR calculated from the angularly resolved BRDF model is compared with the wavelength-dependent reflectance that was measured using a grating spectrometer. An example of this comparison is shown in Fig. 9, where the blue squares are TIRs calculated from the measured BRDFs for a maple leaf, and the red line is the TIR from the spectrometer measurement, also known as the HDR.

EXPERIMENTAL RESULTS

The phase functions explained in the previous section (Eqs. 4 and 5) have been used to model the scattering from the three leaf samples at the different incident angles and wavelengths. Figure 10 shows the reflectance of a red maple leaf at 405 nm at three different incident angles: 5°, 20°, and 60°. The red crosses indicate measured values, and the dotted blue lines are the modeled function. The reflectance of leaves is often modeled as purely Lambertian, but analysis at an incident angle of 60° in Fig. 10 indicates that there is a diffuse component of the scattered light that retains directional coherence.

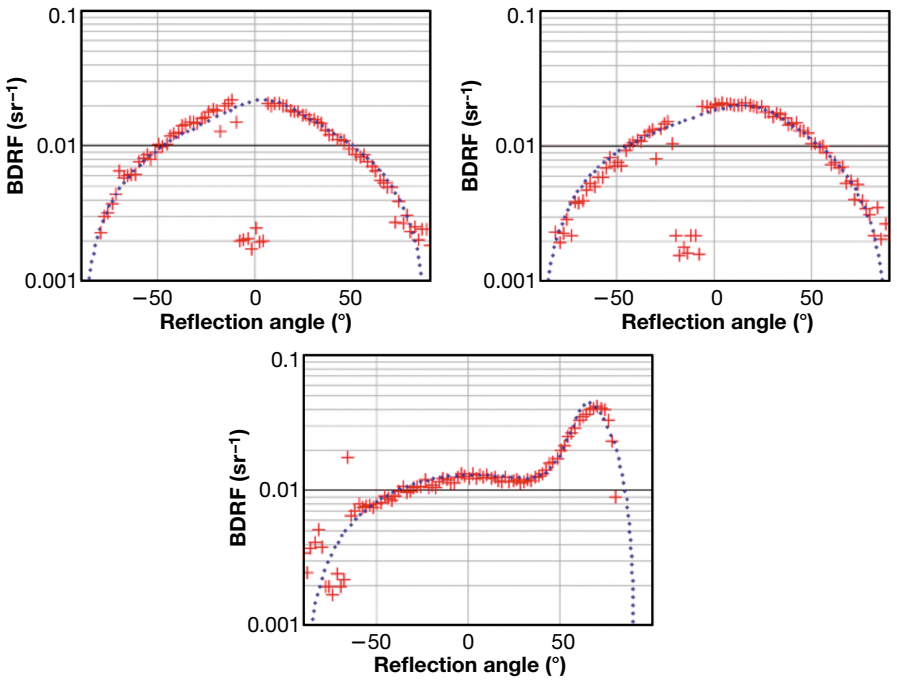

Figure 10. Measured (red crosses) and modeled (blue dotted lines) BRDF for a maple leaf at 405 nm for incident angles (clockwise from top) of 5°, 20°, and 60°. Dropout in experimental BRDF is caused by the detector arm blocking the incident laser for a small range of angles.

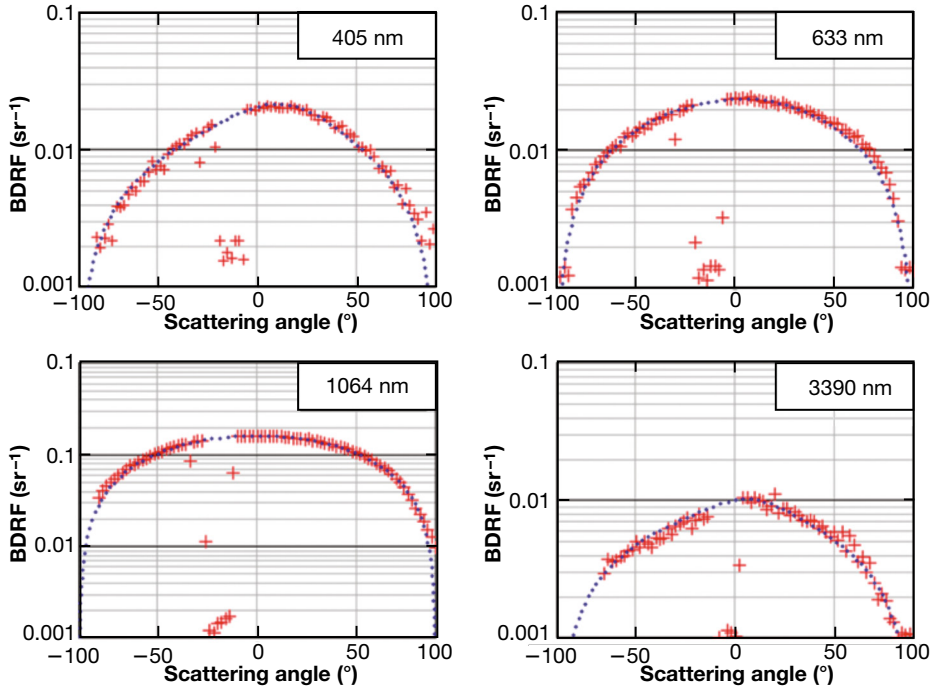

Figure 11. Measured (red crosses) and modeled (blue dotted lines) BRDF for a maple leaf at an incident angle of 20° for wavelengths of 405, 633, 1064, and 3390 nm.

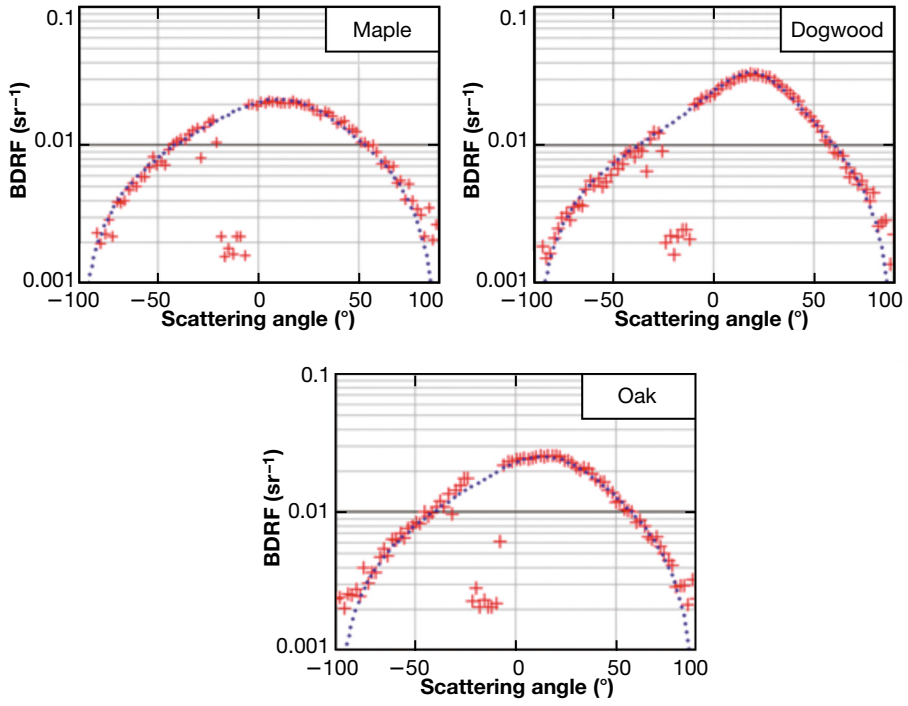

Figure 12. Measured (red crosses) and modeled (blue dotted lines) BRDF for an incident angle of 20° at a wavelength of 405 nm for a maple leaf, a dogwood leaf, and an oak leaf.

Figure 11 shows the BRDF of the red maple leaf at the four different wavelengths: 405, 633, 1064, and 3390 nm. The red crosses indicate measured values, and the dotted blue lines are the modeled function. The BRDF of the three different leaves at 405 nm and for an incident angle of 20° is shown in Fig. 12. Notably, the red maple appears to scatter closest to Lambertian, whereas the dogwood, at 405 nm, has the least Lambertian profile. The parameters used to create the modeled BRDF curves in Figs. 10–12 are summarized in Table 2.

Figures 13 and 14 compare the Kubelka–Munk model fit with the experimental data on the spring/summer dogwood leaf and fall oak leaf, respectively. The model parameters are determined by the reflectance measurement and checked with the transmittance measurement. Good agreement is demonstrated in both cases.

RADIATIVE TRANSFER ANALYSIS

To assess the radiative impact of changes in the BRDF for leaf species, we input into MODTRAN5[18] our fresh and dry maple leaf integrated reflectance (BRDF) values and compare with the default MODTRAN parameterization. Additionally, we investigate the radiative signature calculated from the LOPEX[8] maple leaf parameterization (Fig. 15). The LEAFMOD[10] calculations for reflectance for a variety of leaf thicknesses are plotted in Fig. 15. Because they are comparable in the shortwave (wavelength <2 μm) and minimal LEAFMOD data are available at longer wavelengths, we do not implement these LEAFMOD profiles in MODTRAN.

MODTRAN5 was run for an early-spring, zenith angle of 0° configuration at the APL latitude and lon-

Table 2. Parameters used in modeled fits to BRDF leaf data in Figs. 10–12

Sample	λ (nm)	θ_i (°)	ρ_L	ρ_D	m	α (°)
Maple	405	5	0.045	0.015	2	30
Maple	405	20	0.045	0.015	2	30
Maple	405	60	0.045	0.025	3	25
Maple	405	15	0.030	0.020	2	30
Maple	633	20	0.045	0.015	2	30
Maple	1064	20	0.500	–	–	–
Maple	3390	15	0.02	0.01	2	30
Maple	405	20	0.045	0.015	2	30
Dogwood	405	20	0.023	0.03	2	40
Oak	405	20	0.025	0.03	2	30

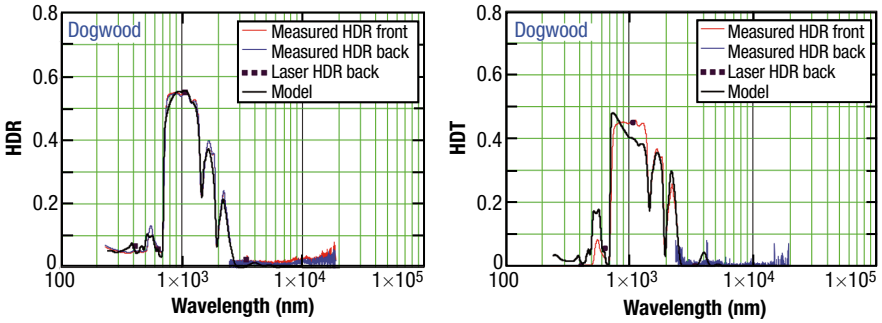

Figure 13. Comparison of Kubelka–Munk model fit to experimental data for a spring/summer dogwood leaf.

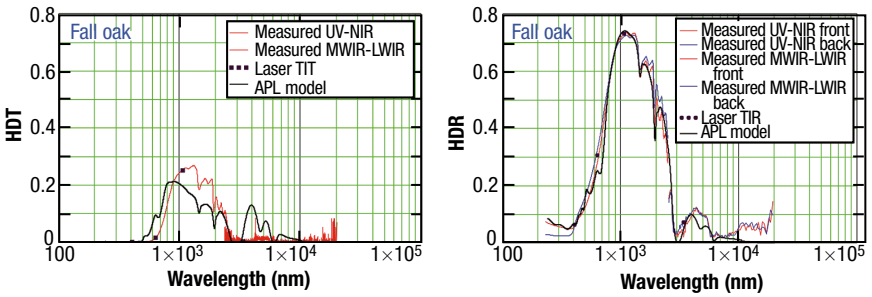

Figure 14. Comparison of Kubelka–Munk model fit to experimental data for a fall oak leaf.

gitude and noon hour. A precipitable water vapor value of 2 cm (NASA MODerate-resolution Imaging Spectroradiometer, MODIS) and column ozone amount of 240 Dobson Unit (NASA Ozone Monitoring Instrument) were implemented with a midlatitude summer meteorological profile and rural aerosol contribution (23-km visibility). MODTRAN cards 4A, 4L1, and 4L2 were implemented. The only change between the analyses of the differing maple reflectances was the specific spectral reflectance file used. Figure 16 displays the results of implementing the APL fresh maple integrated reflectance, derived from the BRDF in grey. The APL dray maple leaf is presented in green. The LOPEX maple leaf in Fig. 15 is shown in magenta, and the default MODTRAN5 maple profile is in black. Minimal to no radiance difference was observed at longer wavelengths (>2.5 μm), despite providing MODTRAN with a more comprehensive spectral reflectance to 10 μm (Fig. 9).

Most notably, the APL leaf models both exhibit greater radiance than LOPEX and MODTRAN default between 400 and 700 nm. There is also a slight enhancement between 1.2 and 1.7 μm from the APL dry maple leaf. If only the dry and fresh APL leaf radiances are examined, we find that the fresh leaf appears to result in a greater radiance than the dry leaf for wavelengths <700 nm, but the dry leaf exhibits a higher radiance from 1.2 to 1.7 μm. Although these radiance signatures are subtle, we have yet to fully investigate the impact on net albedo estimates. We also demonstrate differences from a statistically low sample, and further quantitative impact is necessary with more leaves and leaf clusters. It should be noted that in all instances, the reflectance values supplied are applicable for a single leaf. The impact of canopies has yet to be constrained in this current work but is ultimately critical for a complete understanding of the remotely sensed signature of Earth's surface from space. We anticipate that a small radiative signature from an individual leaf would manifest as a larger signature for a tree or forest, consequentially complicating environmental signature analysis, target detection, and climate analysis. Integrating the full spectra (0–10 μm) plotted in Figs. 16 and 17 results in the following radiances: (*i*) APL fresh maple, 0.0102 W/cm^2-sr, (*ii*) APL dry maple, 0.0101 W/cm^2-sr, (*iii*) MODTRAN default, 0.0099 W/cm^2-sr, and (*iv*) 0.0098 W/cm^2-sr. Relative to the APL dry maple, these percent differences are on the order of

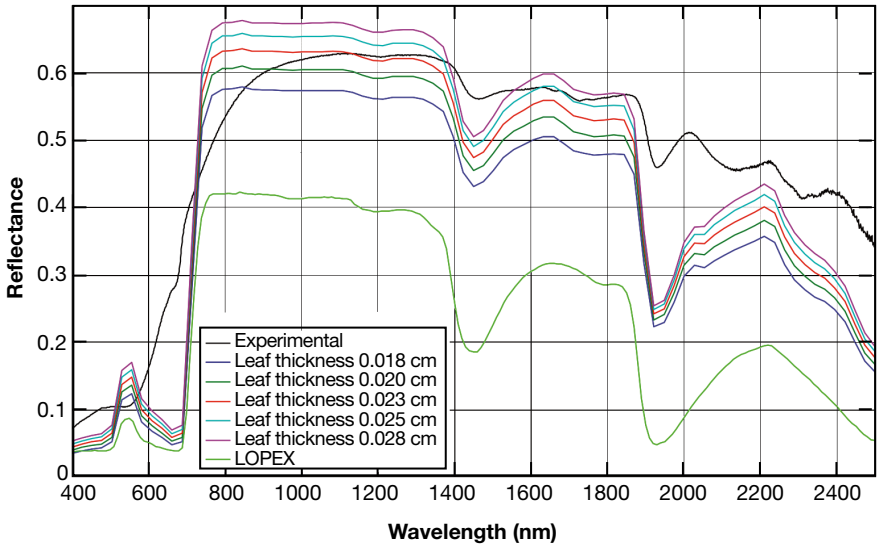

Figure 15. Fresh maple leaf reflectance comparison against the LEAFMOD model and the LOPEX data. The APL experimental results are plotted in black. LOPEX data are presented in green. The other colors indicate reflectances due to different leaf thicknesses.

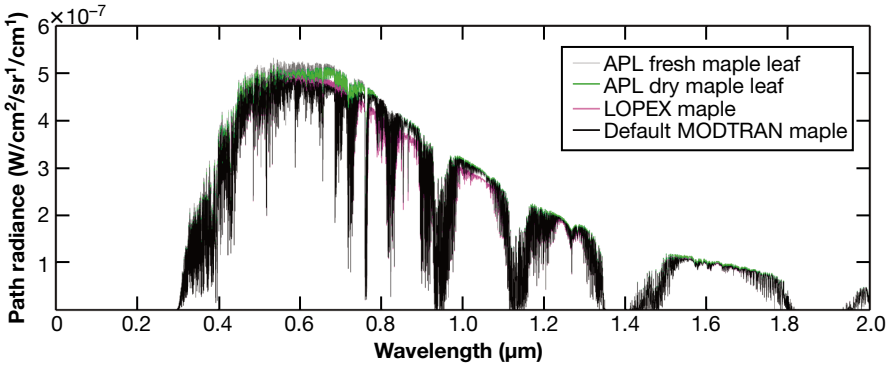

Figure 16. UV-NIR spectral radiance differences between several maple leaf models: APL results (green), default MODTRAN5 (black), and LOPEX model dry maple leaf (magenta). These results were derived by modifying MODTRAN5 parameterization of maple leaf reflectance.

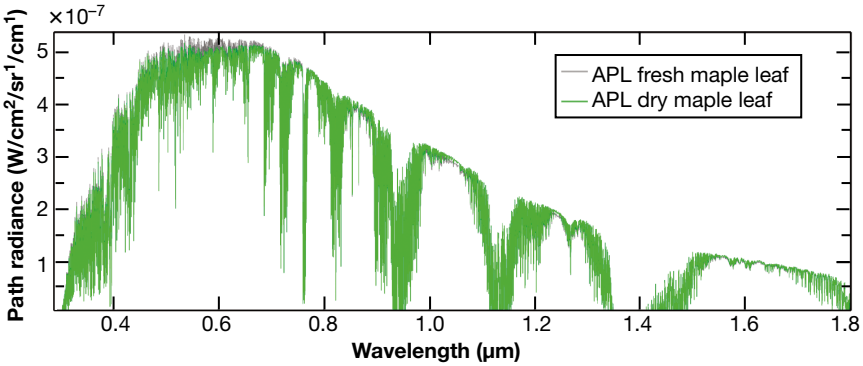

Figure 17. APL dry (green) and fresh (grey) radiance products from MODTRAN5. The fresh leaf appears to have a greater signature from 400 to 700 nm, whereas the dry leaf begins to exhibit and enhancement at 1.2 μm.

1% for the APL fresh maple, 2% for the default MODTRAN case, and 3% for the LOPEX data. Future higher spectral resolution in the APL reflectances may also impact these contributions.

CONCLUSION

As a first step toward creating an improved database of natural Earth surface BRDFs for use in critically decoupling the Earth background from target and atmospheric signatures, we have developed a semiempirical BRDF model for leaves using the APL Air and Missile Defense Sector's BRDF laboratory facility. Sponsored jointly by National Security Space Mission Area and Research and Exploratory Development Department independent research and development funding in 2009, our model was developed for leaves but has potential for broad application. Leaves are easy to acquire, easy to integrate into the existing APL facility apparatus, and highly seasonally and regionally dependent.

Assumed BRDF signatures of leaves impact the atmospheric radiative signature. We have shown that implementing a simple, default MODTRAN model for maple leaf reflectances may underpredict the retrieved radiance signature by 1–3%, based on a statistically limited sample size, and assuming single leaf properties in all comparison analysis. Although this underprediction is small, we anticipate that the retrieved radiance error will increase with increasing leaf number and with the existence of multiple trees. Characterizing the signature of an individual leaf for a specific tree type is important at a fundamental level, prior to identifying the signature of an entire forest. We find that the BRDF model fit the measured BRDF for the leaves. Leaf BRDF is highly dependent on moisture content, chlorophyll content, and orientation (front side or back side). We observe shortwave scattering that seems consistent with scattering off chloroplasts within the individual cells.

At 500 nm, our model reveals a ~0.1 difference in integrated reflection relative to LEAFMOD predictions for maple leaves and, at specific wavelengths, >0.2 difference in reflectance (near 2 μm). A 0.1 difference in reflectance can be easily obtained by observing a fall and spring leaf. Because approximately 0.02–0.05 absolute accuracy is required for climate, biogeochemical, and hydrological models,[6] precise parameterization of seasonally dependent leaf reflectances is important. Ultimately decoupling the radiative signature of leaves from atmospheric signatures and other Earth surface materials will improve APL's environmental characterization capability within the National Security Space, Civil Space, and Air and Missile Defense Mission Areas.

In the real world, we expect leaves to cluster in canopies and on the ground, presenting additional complications that were unexplored in this preliminary research. Consequentially, we move toward incorporating such properties in the APL BRDF facility. We anticipate the next steps to include examination of the BRDF of leaf clusters and coniferous leaf BRDFs. We anticipate this information to be critical for APL to continue participation in NASA Earth climate science and environmental remote sensing and DoD target signature analysis. The fundamental analysis of the radiative impact of leaves would facilitate the development of instrumentation for airborne and space-based platforms for both Civil Space Mission Area and National Security Space Mission Area applications for signature exploitation: natural and man-made object identification and characterization and synthetic paint/material development (to mimic plant/leaf-like characteristics).

ACKNOWLEDGMENTS: We thank summer intern Jessica Makowski for her assistance with the leaf analysis. Thanks to Barry Ganapol and Roberto Furfaro with the University of Arizona for their expertise and assistance with LEAFMOD analysis and comparison. This work was funded through the APL independent research and development program and was co-sponsored by APL's Research and Exploratory Development Department (previously the Milton Eisenhower Research Center) and the National Security Space Mission Area.

REFERENCES

[1]Hudson, S. R., Warren, S. G., Brandt, R. E., Grenfell, T. C., and Six, D., "Spectral Bidirectional Reflectance of Antarctic Snow: Measurements and Parameterization," *J. Geophys. Res.* **111**(D18), 1–19 (2006).

[2]Lee, T. Y., and Kaufman, Y. J., "Non-Lambertian Effects on Remote Sensing of Surface Reflectance and Vegetation Index," *IEEE Trans. Geosci. Remote Sens.* **24**(5), 699–708 (1986).

[3]Hudson, S. R., and Warren, S. G., "An Explanation for the Effect of Clouds over Snow on the Top-of-Atmosphere Bidirectional Reflectance," *J. Geophys. Res.* **112**(D19202), 1–11 (2007).

[4]Oleson, K. W., Bonan, G. B., Schaaf, C., Gao, F., Jin, Y., and Strahler, A., "Assessment of Global Climate Model Land Surface Albedo Using MODIS Data," *Geophys. Res. Lett.* **30**(8), 1443 (2003).

[5]Wang, Z., Zeng, X., Barlage, M., Dickenson, R. E., Gao, F., and Schaaf, C. B., "Using MODS BRDF and Albedo Data to Evaluate Global Model Land Surface Albedo," *AMS J. Hydrometeorol.* **5**(1), 3–14 (2004).

[6]Henderson-Sellers, A., and Wilson, M. F., "Surface Albedo Data for Climatic Modeling," *Rev. Geophys.* **21**(8), 1743–1778 (1983).

[7]Lucht, W., Schaaf, C. B., and Strahler, A. H., "An Algorithm for the Retrieval of Albedo from Space Using Semiempirical BRDF Models," *IEEE Trans. Geosci. Remote Sens.* **38**(2), 977–998 (2000).

[8]Hosgood, B., Jacquemoud, S., Andreoli, G., Verdebout, J., Pedrini, G., and Schmuck, G., *Leaf Optical Properties EXperiment 93 (LOPEX93)*, Ispra, Italy: European Commission (1995).

[9]Grant, L., "Diffuse and Specular Characteristics of Leaf Reflectance," *Remote Sens. Environ.* **22**(2), 309–322 (1987).

[10]Ganapol, B. D., Johnson, L. F., Hammer, P. D., Hlavka, C. A., and Peterson, D. L., "LEAFMOD: A New Within-Leaf Radiative Transfer Model," *Remote. Sens. Environ.* **63**(2), 182–193 (1998).

[11]Huang, C., and Asner, G. P., "Applications of Remote Sensing to Alien Invasive Plant Studies," *Sensors* **9**(6), 4869–4889 (2009).

[12]Su, M. R., Yang, Z. F., Chen, B., and Ulgiati, S., "Urban Ecosystem Health Assessment Based on Emergy and Set Pair Analysis—A Comparative Study of Typical Chinese Cities," *Ecol. Modell.* **220**(18), 2341–2348 (2009).

[13]Berk, A., Bernstein, L. S., and Robertson, D. C., "MODTRAN: A Moderate Resolution Model for LOWTRAN 7," Report prepared for the U.S. Air Force Geophysics Laboratory by Spectral Sciences, Inc., Burlington, MA, http://www.dtic.mil/dtic/tr/fulltext/u2/a214337.pdf (1989).
[14]Kubelka, P., and Munk, F., "Ein Beitrag zur Optik der Farbenstricke" ("An Article on Optics of Paint Layers"), *Z. tech. Physik* 12: 593–601 (1931).
[15]Brown, A. M., Hahn, D. V., Thomas, M. E., Brown, D. M., and Makowski, J., "Optical Material Characterization through BSDF Measurement and Analysis," in *Optical Material Characterization through BSDF Measurement and Analysis*, Proc. SPIE, Vol. 7792, Z.-H. Gu and L. M. Hanssen (eds.), SPIE, Bellingham, WA, pp. 779211-1–779211-11 (2010).
[16]Thomas, M. E., Blodgett, D. W., and Hahn, D. V., "Analysis and Representation of BSDF and BRDF Measurements," in *Optical Diagnostic Methods for Inorganic Materials III*, Proc. SPIE, Vol. 5192, L. M. Hanssen (ed.), SPIE, Bellingham, WA pp. 158–167 (2003).
[17]Duncan, D. D., Hahn, D. V., and Thomas, M. E., "Physics-Based Polarimetric BRDF Models," in *Optical Diagnostic Methods for Inorganic Materials III*, Proc. SPIE, Vol. 5192, L. M. Hanssen (ed.), SPIE, Bellingham, WA, pp. 129–140 (2003).
[18]Berk, A., Anderson, G. P., Bernstein, L. S., Acharya, P. K., Dothe, H., et al. "MODTRAN4 Radiative Transfer Modeling for Atmospheric Correction," in *Optical Spectroscopic Techniques and Instrumentation for Atmospheric and Space Research III*, Proc. SPIE, Vol. 3756, A. M. Larar (ed.), SPIE, Bellingham, WA, pp. 348–353 (1999).
[19]Joseph, R. I., and Thomas, M. E., "How Accurate Is the Kubelka-Munk Theory of Diffuse Reflectance? A Quantitative Answer," in *Reflection, Scattering, and Diffraction from Surfaces III*, Proc. SPIE, Vol. 8495, L. M. Hanssen (ed.), SPIE, Bellingham, WA, pp. 84950I-1–84950I-9 (2012).

APPENDIX

RANDOM DIFFUSE LIGHT PROPAGATION AND KUBELKA–MUNK THEORY

Consider an infinite turbid thin film that is applied to a substrate with a Lambertian surface reflectance of ρ_{Lsub}. Because of random multiple scatter, the flow of random diffuse light flux within the film can only be in two directions perpendicular to the film surface, up and down, because rays to the side ultimately get redirected to the up or down direction. This concept is illustrated in Fig. 18. The downward flux in the film is attenuated by both absorption and scatter. The backscattered component removed from the downward flow is ultimately redirected upward. The same will be true for the net upward flow of flux. Differential equations describing this random diffuse light propagation are stated by Eqs. 9 and 10:[14]

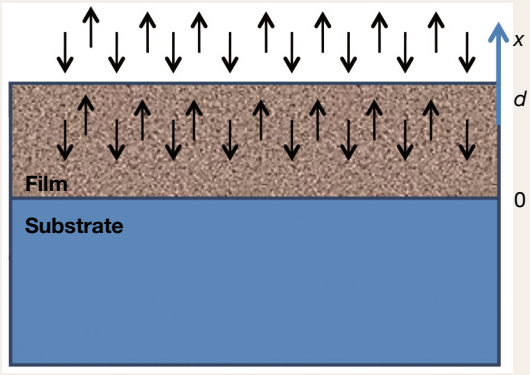

Figure 18. Two-flux diffuse light propagation within a film on a substrate.

$$-d\Phi_{down}(x) = -\left(\beta_{abs} + \beta_{sca}^{back}\right)\Phi_{down}(x)dx + \beta_{sca}^{back}\Phi_{up}(x)dx \tag{9}$$

and

$$d\Phi_{up}(x) = -\left(\beta_{abs} + \beta_{sca}^{back}\right)\Phi_{up}(x)dx + \beta_{sca}^{back}\Phi_{down}(x)dx. \tag{10}$$

The absorption coefficient, β_{abs}, and bulk scatter coefficient, β_{sca}^{back}, are assumed independent of position but depend on wave number, ν. The second term in the preceding equations accounts for random multiple scatter such that the effective forward-to-back scatter ratio is 1, even though the forward-to-back scatter ratio for a single particle may not be 1. It is a source term in the coupled radiation transfer equations. Thus, β_{sca}^{back} in the above equations represents backscattered loss and is one-half the regular scatter coefficient, β_{sca}. The random diffuse reflectance just above the film and the random diffuse transmittance below the film are sought.

Differentiate Eq. 9 and use Eq. 10 to obtain

$$\frac{d^2\Phi_{down}}{dx^2} - \beta^2\Phi_{down} = 0, \tag{11}$$

where $\beta^2 = \beta_{ext}^2 - \left(\beta_{sca}^{back}\right)^2$ and $\beta_{ext} = \beta_{abs} + \beta_{sca}^{back}$. A similar equation is obtained by differentiating Eq. 10, thus

$$\frac{d^2\Phi_{up}}{dx^2} - \beta^2\Phi_{up} = 0. \tag{12}$$

The general solutions to the above homogeneous Helmholtz equations are

$$\phi_{down}(x) = Ae^{-\beta x} + Be^{\beta x} \tag{13}$$

and

$$\phi_{up}(x) = Ce^{-\beta x} + De^{\beta x}, \tag{14}$$

where

$$\beta = \beta_{sca}^{back}\sqrt{\frac{1}{a_L^2} - 1} = \beta_{abs}\sqrt{1 + 2\frac{\beta_{sca}^{back}}{\beta_{abs}}}, \text{ and } a_L = \frac{\beta_{sca}^{back}}{\beta_{ext}}. \tag{15}$$

The random diffuse albedo is a_L and represents the back hemisphere scatter loss. If the forward-to-back ratio is 1, then,

$$\beta_{sca}^{back} = \frac{\beta_{sca}}{2}. \tag{16}$$

For this reason, care must be exercised when comparing the backscatter coefficient in the Kubelka–Munk model to the regular single scatter coefficient and the Kubelka–Munk albedo to the regular albedo. Furthermore, Kubelka–Munk theory is an approximation to a full radiation transfer equation solution in the diffuse limit. It is also expected that the average photon path is greater than the film thickness. Thus, the absorption coefficient should be scaled also. A comparative study produced corrections to bring Kubelka–Munk theory into close agreement with numerical solutions of the radiation transfer equation in the diffuse limit. The Kubelka–Munk or Lambertian albedo is defined in the following manner:[19]

$$a_L = \frac{p\beta_{sca}}{q\beta_{abs} + p\beta_{sca}} = \frac{\frac{p}{q}\beta_{sca}}{\beta_{abs} + \frac{p}{q}\beta_{sca}}. \tag{17}$$

Knowing that $p = 0.5$, it was found that $q = 1.22$.

The random diffuse reflectance and random diffuse transmittance at some distance within the film are defined as

$$\rho_L(x) = \frac{\phi_{up}(x)}{\phi_{down}(d)} \text{ and } \tau_L(x) = \frac{\phi_{down}(x)}{\phi_{down}(d)} \quad 0 \le x \le d. \tag{18}$$

The boundary condition at the interface between the film and the substrate requires

$$\rho_{Lsub} = \left(\frac{\phi_{up}(0)}{\phi_{down}(0)}\right) = \frac{C + D}{A + B}, \tag{19}$$

where ρ_{Lsub} is the Lambertian TIR of the substrate. Solving for the coefficients in Eq. 19, the following results are obtained for a film on an opaque substrate:

$$\rho_L(d) = \frac{b_- - b_+\frac{b_- - \rho_{Lsub}}{b_+ - \rho_{Lsub}}e^{-2\beta d}}{1 - \frac{b_- - \rho_{Lsub}}{b_+ - \rho_{Lsub}}e^{-2\beta d}} \tag{20}$$

and

$$\tau_L(0) = \frac{\left(1 - \frac{b_- - \rho_{Lsub}}{b_+ - \rho_{Lsub}}\right)e^{-\beta d}}{1 - \frac{b_- - \rho_{Lsub}}{b_+ - \rho_{Lsub}}e^{-2\beta d}}, \tag{21}$$

where

$$b\pm = \frac{1}{a_L} \pm \sqrt{\frac{1}{a_L^2} - 1} \text{ (Note: } b_+b_- = 1). \tag{22}$$

In practice, the transmittance is more meaningful when there is no substrate, thus $\rho_{Lsub} = 0$. Then, for the case of a slab (e.g., a window),

$$\tau_L(0) = \frac{2\sqrt{\frac{1}{a^2} - 1}\, e^{-\beta d}}{b_+ - b_-\, e^{-2\beta d}} \tag{23}$$

and

$$\rho_L(d) = \frac{1 - e^{-2\beta d}}{b_+ - b_-\, e^{-2\beta d}}. \tag{24}$$

Using the total power law, the random diffuse absorptance becomes

$$\alpha_L(0) = 1 - \tau_L(0) - \rho_L(d). \tag{25}$$

For the case of an opaque bulk material (such as a rough metallic surface), let d go to infinity. Then the diffuse reflectance reduces to

$$\rho_L(d) = \frac{1}{b_+} = b_-. \tag{26}$$

ANOMALOUS DIFFRACTION APPROXIMATION

ADA yields a computationally efficient and robust approximation to Mie theory in the region of large spherical particles (x large) and for particle refractive index that closely matches the background (van de Hulst). This is often the case in ocean particle scattering and for water-based aerosols. It is based on plane wave propagation and Huygen's principle. It is also assumed that reflection and refraction can be ignored [that is, $(m - 1)$ is small]. Thus the theory emphasizes diffraction and interference effects that often dominate particle scatter phenomenon. Other shapes besides spheres are also possible, and computing the extinction cross-section given a size distribution function is much faster.

The theoretical foundation begins with an incident electric field plane wave illuminating an arbitrarily shaped particle, thus

$$\mathbf{E}_i(z) = E_{i0} \exp(-jk'_0 n_0 z)\mathbf{a}_x. \tag{27}$$

Inside the particle of refractive index n_1 the plane wave becomes

$$\mathbf{E}_s(z) = E_{i0} \exp(-jk'_0 n_1 z)\mathbf{a}_x. \tag{28}$$

Using the above fields, one may determine that the scatter amplitude leads to

$$S(0) = \frac{k'^2}{2\pi} \iint (1 - e^{-jk'_0 n_0 (m-1) z(x,y)}) E(x,y)\, dx\, dy, \tag{29}$$

where $E(x,y)$ represents the projected area of the particle to the incident plane wave, $z(x,y)$ is the path through the particle and $m = \frac{n_1}{n_0}$. In general, m is complex ($m = m_r - jm_i$). The corresponding extinction cross-section becomes

$$C_{ext} = 2\,\mathrm{Re}\left[\iint (1 - e^{-jk'_0 n_0 (m-1) z(x,y)}) E(x,y)\, dx\, dy \right]. \tag{30}$$

For the case of a spherical particle, the chord length is computable. The resulting extinction efficiency is

$$Q_{ext}(x,m) = 4P\,\mathrm{Re}\left[\frac{1}{2} + \frac{e^{-w(x,m)}}{w(x,m)} + \frac{e^{-w(x,m)} - 1}{w(x,m)^2} \right], \tag{31}$$

where $w(x,m) = -j2x(m - 1)$ for a nonabsorbing spherical particle of radius a (ρ real) is

$$Q_{ext}(\rho) = Q_{sca}(\rho) = 2 - \frac{4}{\rho}\sin(\rho) + \frac{4}{\rho^2}(1 - \cos(\rho)), \tag{32}$$

where $\rho = 2x(m - 1)$, $x = k'a = \frac{2\pi n_0 a}{\lambda}$, a is the radius of the spherical particle, n_1 is the refractive index of the particle, and n_0 is the refractive index of the background medium.

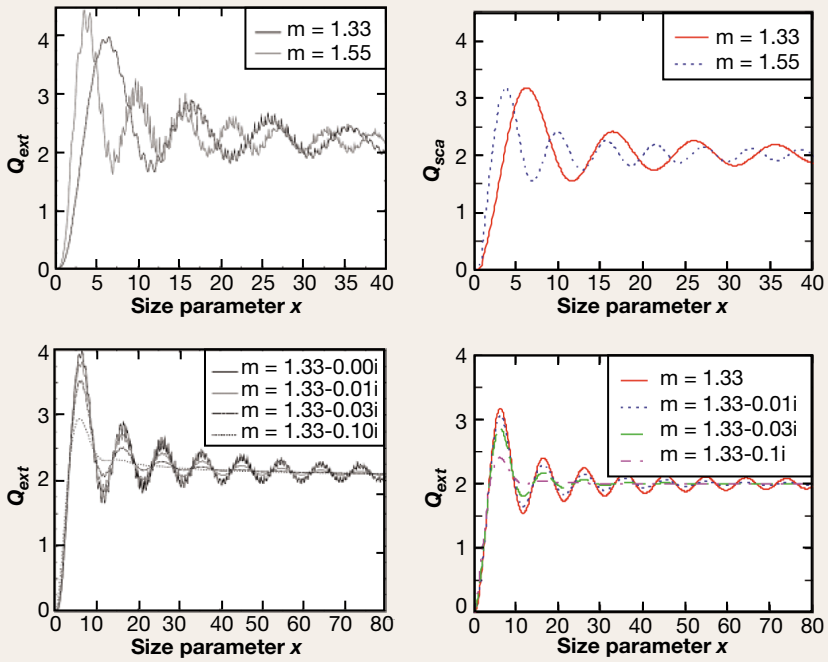

Figure 19. Comparison between Mie theory (left) and ADA (right) for spheres.

The Authors

Shadrian B. Strong, presently in the Air and Missile Defense Sector, is a Co-Investigator (Co-I) for the BRDF independent research and development project. Dr. Strong's expertise is in environmental/atmospheric characterization, remote sensing, and EO/IR performance analysis for space systems. **Michael E. Thomas** is a principal staff engineer in the Air and Missile Defense Sector. He assisted with algorithm development and analysis of BRDF observations. Dr. Thomas is a specialist in electromagnetic theory, optical propagation, and quantum electronics and has research interests in measurement and theoretical modeling of atmospheric propagation and remote sensing, optical properties of solids, and high-pressure gases. **Andrea M. Brown** is in the Asymmetric Operations Sector and is an expert in atmospheric characterization and aerosol modeling. Dr. Brown's expertise has been invaluable in BRDF analysis, algorithm development, and observations. **Elena Y. Adams**, Co-I for the BRDF project, is a systems engineer in APL's Space Exploration Sector and helped with project formulation and research. For further information on the work reported here, contact Shadrian Strong. Her e-mail address is shadrian.strong@jhuapl.edu.

The *Johns Hopkins APL Technical Digest* can be accessed electronically at **www.jhuapl.edu/techdigest**.